

Rose-Hulman Institute of Technology

2011 ASME East Coast HPV Challenge

Unrestricted Class Entry



Presents

ήλιος

(Helios)

Team Officers

Andrew Bomar
Jeffrey Dovalovsky
Drew Robertson
Ethan Rockett
Petras Swissler

Team Members

Rebecca Bowermaster
Simon Burns
Harrison Coons
John Daly
Devon Fritz
Crystal Hurtle
Seth Paris

Jacqueline Simon
Claire Stark
Travis Tatlock
Aaron Vaslow
Patrick Woolfenden
Ariel Young

For more team information visit the team website at:
hpvt.rose-hulman.edu

Contents

1 Abstract.....	1
2 Design and Innovation	1
2.1 Goals	3
2.2 Constraints	1
2.3 House of Quality	1
2.4 Innovation	3
2.4.1 Unassisted Start and Stop.....	3
2.4.1.1 Leaning Tricycle	3
2.4.1.2 Landing Gear	4
2.4.1.3 Removable Fairing	5
2.4.2 Frame Design	5
2.4.3 Rollbar Design.....	6
2.4.4 Smaller Front Wheel.....	7
2.4.5 Universal Joint	7
2.4.6 Fairing Shape Development.....	8
2.4.7 Regenerative Braking.....	8
3 Analysis	8
3.1 Tricycle Width Analysis	8
3.2 Handling Geometry and Torque Steer Analysis	9
3.3 Gear Ratio Selection.....	10
3.4 Wind Condition Analysis	10
3.5 Shock Loading Analysis	11
3.6 Removable Fairing Aerodynamics Analysis.....	11
3.7 Fairing Shape Aerodynamic Analysis.....	12
3.8 Roll-Bar Analysis.....	13
3.8.1 Simple Mechanical Model	13
3.8.2 Finite Element Analysis.....	14
3.9 Frame Analysis	15
3.9.1 Simple Mechanical Model	15
3.9.2 Finite Element Analysis.....	16
3.10 Cost Analysis	18
3.11 Regenerative Braking	18
4 Testing.....	19
4.1 Freestanding Design Testing	Error! Bookmark not defined.
4.2 Optimal Cadence Testing	19
4.3 Seat Position	21
4.4 3-Dimensional Motion Capture Testing	22
4.5 Fairing Mounting Testing	22
4.6 Kevlar Zylon Testing	23
4.7 Roll Cage Testing	23
4.8 Universal Joint and Stability Testing	24
4.9 Speedplay Frog Cleats	25
5 Practicality	25
5.1 Conditions	25
5.2 Visibility.....	26
5.3 Utility Features.....	26
5.4 Special Features	26
6 Safety	26
6.1 Communication.....	27
6.2 Rider Elbow Protection	27
Appendix 1 Cost.....	28
Works Cited	29

1 Abstract

During the 2010-2011 competition year, the Rose-Hulman Human Powered Vehicle Team designed, tested, and constructed a new vehicle, the Helios, for entry into the Unrestricted Class of the 2011 Human Powered Vehicle Competition (HPVC). This process of creating the Helios was guided by the team's mission statement for 2010-2011, written below:

“For the 2010-2011 competition year, The Rose-Hulman Human Powered Vehicle Team will pursue continued success in the Unrestricted Class of the ASME sponsored HPVC by using all available resources for design, testing, and construction, building on past experience by communicating with alumni, and focusing all endeavors on meeting the most important design goals.”

The team performed interviews to help generate a list of goals and constraints for design of the Helios. Metrics were developed to evaluate how well different designs would satisfy these needs. The team also determined the importance of each need and benchmarked designs against the 2010 Ragnarök and other successful Human Powered Vehicles (HPVs). This information was summarized in a House of Quality (HoQ) to help streamline the decision making process.

Analysis was performed to predict the performance of several of the vehicle's systems. The deflection of the rollover protection system (RPS) was estimated analytically and using Finite Element Analysis (FEA) per the 2011 RPS requirements [1]. Computational Fluid Dynamics (CFD) was used to refine the shape of the vehicle's fairing to reduce the amount of drag on the vehicle and to predict the performance of the final vehicle. Statistical analysis of historical wind data from the competition sites aided the CFD analysis.

Physical testing of a mock-up of the Helios's RPS was performed per the 2011 RPS requirements [1]. The Helios's RPS was found to exceed all HPVC requirements. Performance testing was conducted on multiple prototypes to determine the best design for meeting the free-standing requirement of the Unrestricted Class. A $\dot{V}_{O_2,max}$ test was performed to help identify the best riders and to determine the optimal cadence of our riders while riding a recumbent bicycle. Ergonomics testing was used to help determine a seat back angle for the Helios, and tests of possible rib structures and roll bar mounts were performed to aid in the design of the frame and fairing.

Three-view and isometric drawing of the Helios are included with the vehicle description form.

The design of the Helios combines speed and practicality into an HPV in many new ways. The end result of the work performed by the Rose-Hulman team during this competition year is a vehicle that brings the field of HPVs closer to the ideal vehicle for human powered transport.

2 Design and Innovation

2.1 Constraints

A list of constraints for the vehicle's design was also generated to help the team decide upon the best design for the HPV. These constraints include the requirements listed in the official 2011 HPVC rules. Additional constraints were based upon the rules of Human Powered Race America, in which the team also competes, and the Rose-Hulman team's own consideration for safety. Table A outlines these constraints.

Table A: 2011 Vehicle Constraints

15 ft (4.57 m) minimum turning radius	Rear-view mirrors
Braking from 15 to 0 mph (24.24 to 0 kph) in < 20 ft (6.10 m)	Rider protection from sliding/abrasion
Independent and redundant braking system	No exposed carbon fiber near rider
Cargo area able to hold groceries	Safety harness
Roll bar supporting 600 lb _f (2.67 kN) top load with elastic deflection less than 2 in (5.1 cm)	
Roll bar supporting 300 lb _f (1.33 kN) side load with elastic deflection less than 1.5 in (3.8 cm)	

2.2 House of Quality

To design a vehicle to better meet the needs of the Unrestricted Class, the team used a quality function deployment to re-analyze the significance of the various design considerations in light of the lessons learned this past year. Using the constraints listed in section **Error! Reference source not found.**, a list of need statements and metrics were produced. These, in turn were used to generate a House of Quality (HoQ), shown in Table B.

2.3 Goals

After analyzing the house of quality the team generated a list of goals, which are listed in Table C.

Table C: 2011 Vehicle Goals

Minimize weight	Is aesthetically pleasing
Maximize stability	Maximize rider power output
Allows awareness of surroundings	Improve vehicle durability
Reduce manufacturing tolerances	Maximize aerodynamic efficiency
Maximize rider practice time	Minimize Rider Injury

2.4 Innovation

2.4.1 Unassisted Start and Stop

Meeting the requirement that the rider be able to start and stop unassisted received a high importance score in the HoQ, described in Section 2.2. The team built prototypes of several possible designs that would meet this requirement in order to conduct performance tests to determine the best design.

2.4.1.1 Leaning Tricycle

One possible solution identified by the team is a leaning tricycle configuration, similar to that employed successfully in the 2010 Ragnarök. A leaning tricycle has two rear wheels, mounted in such a way that the frame, fairing, and rider of the vehicle can lean relative to the ground. This allows the rider to take corners at speed by leaning, in the same way the rider would take corners on a bicycle. However, a mechanism can also be included to fix the position of the rear wheels relative to the frame, holding the vehicle upright. By engaging and disengaging this mechanism during transitions between high and low speeds, the rider has the stability benefits of both two- and three-wheeled vehicles.

The design employed on the 2010 Ragnarök was a four-bar mechanism that made the wheels lean with the vehicle. This year, the team explored the possibility of a single beam design, in which the wheels stay upright when the bike leans. Figure 1 shows the two tested leaning tricycle designs.



Figure 1: Prototype of Four-Bar (left) and Single-Beam (right) Tilting Tricycle Assemblies

A single beam design is much simpler, improving manufacturability, weight, and aerodynamics. Interference between the fairing and wheels is one reason why a four-bar mechanism was pursued for the 2010 Ragnarök, but the 2011 ASME HPVC rules allow the team to resolve this issue by increasing the width of the wheels 9.8 in (0.25 m) to 39.4 in (1 m). This also increases stability when the vehicle is fixed upright, as is discussed in Section 3.1. Because landing gear is more aerodynamic, this design is intended as a backup on the Helios.

2.4.1.1.1 Locking Mechanism

The leaning tricycle system requires a mechanism to lock the vehicle in a vertical position. To improve stability and decrease complexity over the 2010 Ragnarök, a new method of locking the vehicle in an upright position was selected for the Helios.

Many of the prior tilting tricycle designs examined in designing the 2010 Ragnarök utilized disk brakes to prevent rotation, but provided inadequate torque to hold the vehicle upright when not perfectly vertical. This is especially

problematic because the rider cannot easily tell when the vehicle is vertical. The design of the 2010 Ragnarök solved this issue by using a pin to lock the vehicle in place, providing sufficient force and ensuring correct alignment. However, it was challenging for riders to learn to use this system because the pin engaged and disengaged very suddenly. Additionally, the pin design could only lock in one position, limiting its usefulness when stopping on a slope.

For the 2011 Helios, new designs were developed to lock the leaning tricycle without the drawbacks of either of the standard disk brake or pin designs. Three candidate designs were considered: a pin design with independent suspension, a brake with a force multiplier, and a brake with a large disk. The pin and suspension design relied on the suspension enabling the vehicle to tilt somewhat while locked, providing the rider with feedback of when it was balanced. This design was eliminated because it was less stable in turns and it added unnecessary complexity, violating the design goals that it be reliable and easy to repair. The force multiplier design used hydraulic, rather than mechanical, brakes to achieve a larger force on the brake disk. The large brake disk design used a larger moment arm to keep the vehicle upright. Although the addition of a large brake disk increases the drag force on the vehicle, it was selected to be prototyped because it permits greater standardization of parts than the use of a hydraulic brake.

A system with an 8.5 in (21.6 cm) brake disk was prototyped and proved effective at keeping the rider upright while being simple to engage and disengage.

2.4.1.2 Landing Gear

Another option considered for allowing the rider to freely stop and start the bike was a landing gear mechanism. The landing gear would act like training wheels at low speeds but will be retracted by the rider to allow operation at high speeds. The primary advantage of landing gear is that it is the most aerodynamic of all options, folding up inside the fully faired vehicle to minimize drag.

Two possible landing gear designs were identified. The first design was a swinging arm design, in which the landing gear would be actuated by swinging an arm outwards from the vehicle. The second design identified was a telescoping landing gear. With this design, the landing gear is actuated linearly.

2.4.1.2.1

A prototype of the swinging arm design was constructed. A push-pull cable was used to actuate the landing gear. The handle used by the rider was placed in a slotted sleeve. This allowed the rider to turn the handle in order to lock it in the extended or retracted position, similar to the bolt on a rifle. Figure 3, below, shows the prototype landing gear and latching handle.



Figure 2: Landing Gear Prototype with Latch Mechanism

The swinging arm design proved to be difficult to actuate due to the large moment of inertia of the arm.

2.4.1.2.2

The Telescoping will use two hollow nesting members and will be actuated by use of a brake cable as is demonstrated in Figure 3.

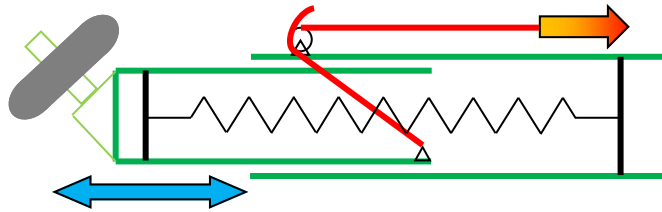


Figure 3: Telescoping landing gear

This design will allow a rider to quickly retract the landing gear by releasing the cable, as was requested by our riders. At this point the spring will cause the smaller of the two members to shoot up into the larger member, which will be situated entirely in the fairing to protect the mechanism from damage in the event of a crash. Telescoping landing gear will be pursued for the Helios.

2.4.1.3 Removable Fairing

The third considered option for unassisted start and stop is a removable fairing. This design constitutes a fairing with large, removable sections to allow the rider to place their feet on the ground when stopped. A rider is able to more quickly enter and exit an un-faired vehicle, and the decreased weight improves acceleration. In the selected design, a tail box and nose cone are used to reduce drag, based on the results of CFD described in Section 3.6. This partially faired configuration will be used during the Utility race, when starting and stopping occurs frequently. The full fairing will then be attached for competition in higher speed events such as sprint and speed endurance. Utilizing the full fairing additionally requires one of the other methods of unassisted start and stop to be implemented, such as a landing gear. The roll bar was chosen as the primary attachment point between the steel frame and composite fairing because it is the strongest and stiffest part of the fairing, which allows the mounting system to contribute to the rollover protection system.

2.4.1.4 Concept Selection

The previously described designs were prototyped and tested, and a concept scoring exercise was completed to determine which design would be pursued. Criteria were developed for each of the four events, and each design was scored on each criterion. Table ____, below, shows the summed scored that each design received for each event.

Event	Weight	Tilting Trike		Landing Gear		Removable Fairing
		Pin	Brake	Swinging	Telescoping	
Design Event	(10% of 40pts)	18	21	21	24	24
Sprint Event	(20 pts)	18	15	24	24	24
Utility Event	(20 pts)	12	12	18	18	21
Endurance	(20 pts)	18	15	24	24	24
Total Score		8.9	8.4	11.7	12.1	12.4

The events were weighted to calculate a total score for each design. The design event was only give a weight of 10% of the allotted 40 points because this design decision was found to only effect about 10% of the points available from the design event. It was found that the removable fairing design was the most favorable, due to its modularity. However, another design would be needed to allow the Helios to start and stop unassisted when the full fairing was on the vehicle. A telescoping landing gear was chosen for this purpose.

2.4.2 Frame Design

In moving from a structural fairing design, the team needed to design its first stand-alone frame since 2007. To assist the design process, a list of goals was made, as shown in Table D.

Table D: Frame Goals

- | | |
|-----------------------------------|------------------------------|
| Achieve a Factor of Safety of 2 | Decrease Weight |
| Minimize Manufacturing Difficulty | Optimize Rider Leg Extension |
| Easy to Attach Fairing | Increase Rider Comfort |

To ensure adequate clearances, a maximum tubing size of 2 inches was chosen. After the simple mechanical model analysis described in Section 3.9.1 was performed, chromoly steel was chosen as the frame material. With these aspects of the design set, a model of the frame was drawn in SolidWorks and FEA was performed in Ansys, as described in Section 3.9.2. Preliminary frames used round tubing and standard rear bicycle forks, but round tubing did not provide the strength needed, and standard bicycle forks did not allow for sufficient mounting of the RPS. Switching to 1 in x 2 in (25 mm x 51 mm) rectangular tubing allowed for a great increase in strength while reducing overall weight, and also allowed for the frame to be much more easily assembled. A proper support system for the RPS was eventually devised to provide both vertical and horizontal support to the mounting tubes.

2.4.3 Roll Bar Design

To ensure the safety of the rider while maintaining a streamlined shape for the vehicle, a composite roll bar was designed. The analyses described in Section 3.8 indicated that this would meet the 2011 RPS specifications. This was then confirmed by the testing described in Section 4.6. The manufacturing method used by the team involves fabricating left and right halves and seaming them together, so the roll bar had to be manufactured in this manner Figure 4, below, diagrams the layers in the roll bar, with the seam depicted in the middle.



Figure 4: Roll Bar Seam Layers

The thick region portrayed in the center of Figure 4 shows the materials used to seam the two halves of the roll bar. In accordance with research conducted in 2009, the composite layers overlap by at least 2 in.

The team first tested simply bonding the frame to the roll bar using epoxy, as described in Section 4.4 was tested and found to be inadequate. Another idea was to simply bolt the frame to the composite roll bar, as the team's roll-bar tests since 2008 had all successfully utilized bolts to mount the roll bar, but the team was concerned about damage to the bolt heads in a crash. As a result, the method shown in Figure 5 was developed.

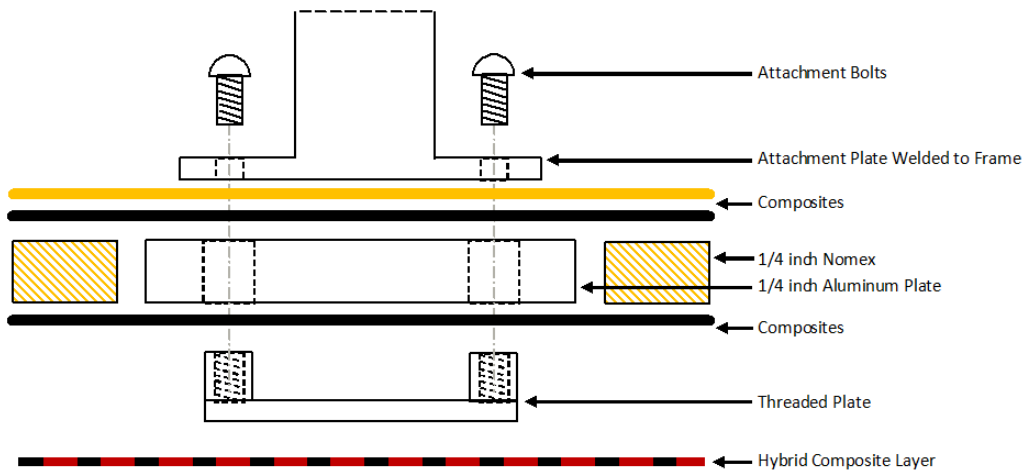


Figure 5: New method of attaching frame to RPS.

In this design, bolts are used to clamp down on the structural composite layers, while the abrasion resistant carbon-Kevlar hybrid protects the mounting system from damage. Due to concerns that the Nomex would crush, a 0.25 in

aluminum plate takes the place of the Nomex in the clamped region. This design was tested with the rest of the RPS as described in Section 4.6.

2.4.4 Smaller Front Wheel

Front wheel size, crank length, and seat position were identified as having related impacts on the vehicle performance. Concept scoring was then utilized to determine the optimal configuration. ISO 35x349 and ISO 35x590 small and large wheels, 135 mm and 175 mm cranks, and 30° and 50° seat angles were considered. Based on their predicted impact on each criterion, these were scored relative to a baseline design utilizing an ISO 28x451 medium-sized wheel, 155 mm cranks, and a 40° seat angle. Weights are based on the importance values determined in the House of Quality, discussed in Section 2.2. The concept scoring matrix is shown in Table E

Table E: Concept Scoring Matrix

		Concept						Baseline
		Front Wheel		Crank		Seat Position		
Selection Criteria	Weight	Small	Large	Short	Long	Reclined	Upright	Intermediate
Forward Distance for Sight of Ground	4	7	4	7	4	4	7	5
% Maximum Power Producing	4	5	5	1	9	4	6	5
$c_d A$	3	7	3	6	4	6	4	5
Cross-wind $c_d A$	3	8	2	6	4	6	3	5
Rider Satisfaction with Handling	5	4	6	5	5	5	5	5
Rider Satisfaction with Ergonomics	3	6	4	4	6	7	3	5
Weight	2	6	4	5	5	5	5	5
Vehicle Volume	1	6	3	6	4	6	4	5
	Total Score	149	104	121	133	130	121	125

The concept scoring indicated that ISO 35x349 wheels, 175 mm cranks, and a reclined seat position are each preferred. When used in combination, the small front wheel overcomes the disadvantages of the long cranks and reclined seat position for a slight reduction in handling performance. Because rider satisfaction with handling was identified as a priority, making this tradeoff required putting additional effort into the design of the steering geometry.

This configuration was then used to establish actual seat, bottom bracket, and wheel positions, and to validate that these positions would satisfy the selection criteria.

2.4.5 Universal Joint

The steering geometry analysis described in Section 3.2 indicated that a large negative fork offset was required to achieve good handling characteristics, which would result in torque steer and chain derailment problems. Three options were considered to fix this issue: rear wheel drive, a bottom bracket that moves with the fork, and a universal joint in the drive train. The first two of these solutions seek to eliminate the bend in the drive train: rear wheel drive was rejected because of chain routing concerns, while the moving bottom bracket was rejected for requiring major concessions to aerodynamics. Although more complex to manufacture, a universal joint solution was selected for reliability and aerodynamics.

While designing the universal-joint mid-drive system, we determined that the most important factors were reliability, efficiency, and low weight. The bend in the universal joint must be coaxial with the head tube to ensure proper function. Because precise tolerances are required, the parts were rough cut using a water-jet cutter, and then finished on a milling machine. In order to keep weight down, the majority of the parts were made from aluminum. A universal joint was selected that could transfer the predicted calculated torque at the operating angles needed for steering. Needle roller bearings were selected to support the universal joint because of their small profile and radial load capacities. This design was then prototyped and refined, as described in Section 4.7.

2.4.6 Fairing Shape Development

The fairing was designed to minimize aerodynamic drag without interfering with the rider’s motion or vision. To ensure that appropriate clearances were maintained, planar curves were generated from data collected using a three-dimensional motion capture system and imported into SolidWorks to create a wire frame model of the space required by the rider. This motion capture process and generation of planar curves, described in Section 4.3, quickly created a more accurate model of the rider space than attempts to model the rider by hand, and fairing cross-sections could be more easily drawn on the same planes as the rider cross sections.

Additional fairing shape constraints were determined based on past experience and engineering considerations. Large integrated windshields were ruled out due to visibility concerns and the potential for elevated internal temperatures. A maximum lean angle of 45° was chosen to ensure that the fairing does not strike the ground during turns. A fairing model was designed to meet these constraints, and an iterative design process was conducted using Computational Fluid Dynamics (CFD) software to analyze and refine the model as described in Section 3.7.

2.4.7 Regenerative Braking

A regenerative braking system was designed for use in the Helios. Weight and complexity concerns led to the selection of an electronic system. An electric motor would be used as a generator to store energy in either a battery or capacitor, and then use that energy later to propel the vehicle. A controller would be needed to regulate the system. In order to keep the design simple and easily removable, the system was designed to mount behind the seat and connect to the rear wheel via a single-speed chain drive.

The system would cost approximately \$200, and would add approximately 20 lbs to the weight of the bike. However, because analysis conducted in Section 3.11 indicated that competition requirements prevent this system from being utilized effectively, the system was not implemented.

3 Analysis

3.1 Tricycle Width Analysis

In order to improve rider satisfaction with handling, the effect of rear wheel width on the stability of a non-leaning delta tricycle was analyzed. This analysis would predict the performance of a leaning tricycle system when the tricycle is locked upright, or the performance of a landing gear system with the wheel deployed. It would also help determine the necessary width of the leaning tricycle system and length of the landing gear.

To analyze the effect of wheelbase width on turning capability, a free-body diagram of the vehicle was drawn as shown, representing a vehicle in the sharpest turn possible without tipping. The diagram, shown in Figure 6, uses the reference frame of the vehicle, where r is the radius of curvature of the vehicle’s path.

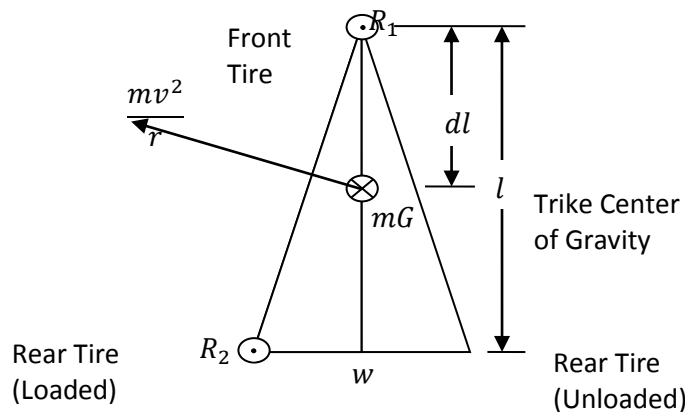


Figure 6: Tricycle Free Body Diagram

Summing the moments about a line from the front wheel to the outside back wheel and equating the sum to zero yielded Equation 1.

$$Gdr^2w + v^2hw - v^2hdw - 2v^2h\sqrt{-l^2d^2 - l^2 + 2l^2d + r^2} = 0 \tag{1}$$

Solving for the width yielded Equation 2.

$$w = \frac{2v^2h\sqrt{-l^2d^2 - l^2 + 2l^2d + r^2}}{Gdr^2 + hv^2 - v^2hd}$$

This equation gives the minimum width, w , in terms of the velocity, v , turn radius, r , acceleration due to gravity, G , wheelbase length, l , center of gravity height, h , and fraction of weight supported by the rear wheels, d . When the opposite rear tire is about to leave the ground, there are no forces on it, and the moments sum to zero.

A MATLAB program was then written to produce a contour plot of the required width over a range of speeds and turn radii, given a constant wheelbase length and center of gravity location. The results are as shown in Figure 7.

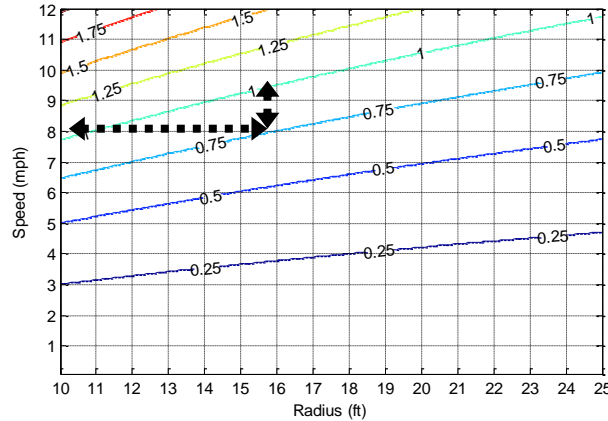


Figure 7: Required Tricycle Width in Meter

As indicated by the dashed arrows on Figure 7, an increase in rear width from 29.5 in (0.75 m) to 39.4 in (1.0 m) would lower the minimum turn radius by around 6 ft (1.8 m) for a given speed, or increase the allowable speed for a given turn radius by around 1.5 mph (0.67 m/s).

Based on these preliminary results, it was determined that the increased stability provided by a wider wheelbase would outweigh the disadvantages in maneuverability and weight.

3.2 Handling Geometry and Torque Steer Analysis

The vehicle steering geometry was designed using formulas from Dr. William Patterson's "The Chronicles of the Lords of the Chainring" [2]. Low speed steering input force was reduced by making the headset more vertical, and a negative fork offset was applied to maintain trail. Rather than simply minimizing the torque steer resulting from chain tension in a front wheel drive system during manufacture, the torque steer, τ , was modeled ahead of time using Equation 3,

$$\tau = T \|\vec{F}\| \cdot \|\vec{V} \times \vec{D}_N\| \|\vec{D}_N\| \quad 3$$

Where T is the magnitude of the chain tension to the wheel, F is the direction of the chain, V is the rotating axis of the steer tube, and D_N is the vector normal to both F and V . As the torque applied by the rider varies throughout each pedal stroke, the magnitude of τ oscillates at double the rider's cadence. Four important conclusions were drawn from this:

- 1) The torque steer is zero when the chain path is coplanar with the steer axis, not just parallel. Minimum torque steer is achieved across all steering deflections by bringing the contact point of the drive chain and drive gear near to the head tube despite the chain not being parallel to the head tube.
- 2) Torque steer does not pull the wheel to a strait forward position. The position it pulls the wheel to is also dependent on the gear selection on the cassette.
- 3) Torque steer does not change linearly or symmetrically with the steering deflection.
- 4) The peak of the torque steer response to the handlebars is greater than the sum of both the static and velocity based responses due to the steering geometry in both starting situations, and in sharp turns.

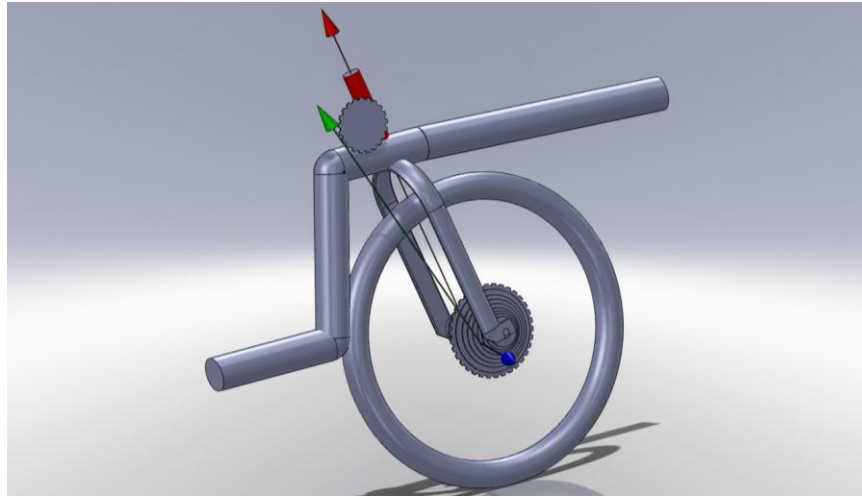


Figure 8: The front wheel of a recumbent single track vehicle. The red vector is V , the green vector F , and the blue vector D_N .

Torque steer is time varying with a relatively low frequency, so it cannot be modeled as a constant bias in the steering. Further analysis indicated that at 400W, the steering forces needed to correct for torque steer range from -14 lb_f (-64 N) to 17 lb_f (77 N). This revealed that final tuning of trail done in previous years had actually served to minimize torque steer in starting gears, instead of for steady state handling. Even if riders were able to correct for these forces, doing so would result in earlier rider fatigue. Chain derailment due to the large range of motion of the hub was also a major concern. Based on this analysis, the team decided to add a universal joint to the drive train, as described in Section 2.4.5.

3.3 Gear Ratio Selection

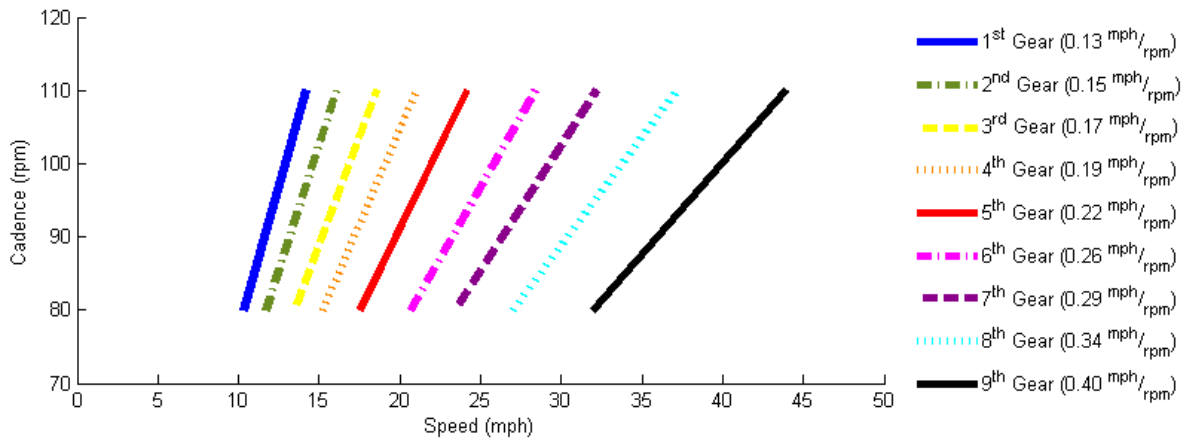


Figure 9: Available Cadence to Speed Ratios

The team's goal in choosing gear ratios was to have the ability to reach 45 mph (72 km/h) while maintaining a cadence between 80 rpm and 110 rpm between speeds from 10 mph (16 km/h) to 40 mph (64 km/h). The team has previously attained speeds of 45 miles per hour, but only the sprint race requires speeds that high. Therefore, the gear ratio selection was focused on maintaining a reasonable cadence at speeds encountered in the utility and endurance races. To reach 45 miles an hour (72 km/h) at a cadence of 110 rpm requires a gear ratio of 8.6:1.

In order to use standard bicycle parts, the cranks are fixed at 60 teeth and the cassette at the wheel has an 11 to 34 sprocket. A 13 tooth input sprocket and 20 tooth output sprocket were selected. This gear ratio in top gear is 8.4:1, which is slightly lower than the ideal for reaching 45 mph (72.4 km/h) but provides better low end performance allowing faster acceleration.

3.4 Wind Condition Analysis

The combination of a vehicle's motion and the motion of the wind produce an apparent wind angle, or angle of attack. As the vehicle moves faster, a cross-wind becomes less significant. In order to ensure that the fairing design is effective

at likely apparent wind angles, a MATLAB program was used to determine the weighted probability of each wind angle, using the method described in the 2010 design report [3]. The expected mean wind speeds for Indianapolis, Indiana and Bozeman, Montana were found to be 9.9 and 6.1 mph, respectively, based on National Weather Service data[4]. Based on the vehicle speeds encountered in last year's competitions, the expected vehicle speed distributions were updated as shown in Equation 4,

$$\text{Speed Probability} = 2f(V_{\text{vehicle}}, 19, 2.5) + 2f(V_{\text{vehicle}}, 14, 3.5) + H(45 - V_{\text{vehicle}}) + H(35 - V_{\text{vehicle}}) \quad 4$$

with terms estimating speed distributions for the endurance events and the male and female sprint events. $f(V_{\text{vehicle}}, \mu, \sigma)$ is the normal distribution with mean μ and standard distribution σ , and H is the Heaviside function. The cumulative distribution of the apparent wind angle is shown in Figure 10.

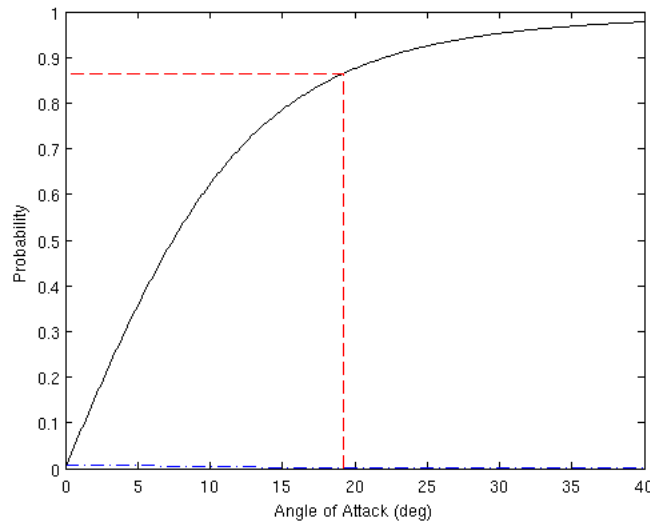


Figure 10: Wind Angle Significance

This distribution indicates that 86% of the expected winds occur at an apparent angle of less than 19.2°, which corresponds to a 7 m/s (15.7 mph) cross wind at 20 m/s (44.7 mph). Based on this analysis, fairing designs were tested in crosswinds ranging from 0 to 19.2°, as described in Section 3.7.

3.5 Shock Loading Analysis

In order to select an appropriate shock loading factor for the vehicle, the magnitude of impact loads the vehicle was likely to encounter were analyzed. Under normal use conditions, forces sufficient to bottom out the rim of a wheel on a road surface are rarely encountered, so this loading condition was analyzed as an estimate of the probable dynamic loading.

For this analysis, an ISO 32x349 wheel was modeled as pressing against a 120 degree corner, with a rectangular contact patch. The tire was assumed to be inflated to 90 psi, and to remain the same width as it was compressed. The projected contact patch area (normal to the load on the hub) was found to be 4.26 in², for a force of 427 lb_f. The maximum static loading on the front wheel was found to be 156 lb_f. The shock loading factor of 2.75 was increased to 3.0 to account for model inaccuracies, and applied prior to calculating safety factors on the frame.

3.6 Removable Fairing Aerodynamics Analysis

To aid in deciding whether to implement a removable fairing, models of various portions of the fairing were analyzed. Since the purpose was only to get a rough idea of how well various configurations would perform, it was sufficient to use rough models at low simulation accuracy. The configurations modeled are shown in Figure 11.

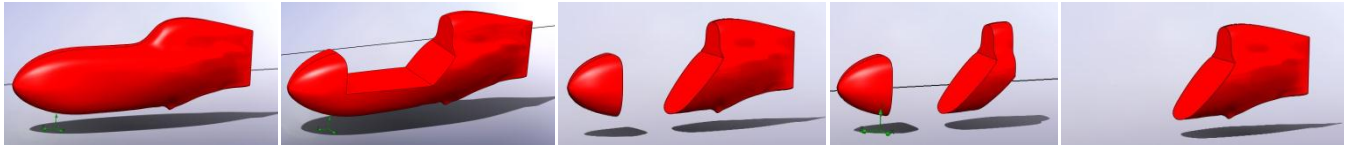


Figure 11: Simulated Configurations (left to right): Fully Faired; Tub; Nosecone and Tailbox; Nosecone; Tailbox

Each model was tested at 20 m/s (44.7 mph) with 0, 3 and 6 m/s (0, 6.7, and 16.4 mph) cross winds. The drag forces for each model are summarized in Table F.

Table F: Partial Fairing CFD Results

Crosswind, m/s (mph)		Drag Force, <i>lb</i> (<i>N</i>)			
		0 (0)	3 (6.7)	6 (13.4)	Average
Model	Full Fairing	2.5 (11)	2.9 (13)	2.5 (11)	2.6 (12)
	Tub	6.5 (29)	8.5 (38)	6.7 (30)	7.3 (32)
	Nosecone and Tailbox	7.6 (34)	8.3 (37)	11.2 (50)	9.1 (40)
	Nosecone	9.2 (41)	11.5 (51)	16.2 (72)	12.3 (55)
	Tailbox	10.3 (46)	11 (49)	7.6 (34)	9.7 (43)

Based on the results of this testing, it was determined that the advantage to stopping and starting provided by a nosecone and tailbox configuration was likely to be greater than the aerodynamic advantage afforded by a tub configuration.

3.7 Fairing Shape Aerodynamic Analysis

To develop an aerodynamic fairing shape which met all constraints in Section 2.4.6, CFD analysis was conducted on each fairing model using SolidWorks Flow Simulation 2010 and the results were used to improve each model. The head wind for all tests was 20 m/s (44.7 mph). Based on the model of expected wind angles, each model was initially tested at 0, 3, and 6 m/s (0, 6.7, and 13.4 mph) cross wind. Models which performed well under these conditions were then simulated at 1 m/s (2.2 mph) increments up to 7 m/s (15.7 mph) cross wind. These results were then multiplied by the probability of encountering their respective apparent wind angles, as determined in Section 3.4, and trapezoidal integration was used to determine the mean drag force on each model.

The location and relative movement of the ground were incorporated in the CFD simulations. Symmetry was used in simulations without cross wind, but was not applicable in simulations with cross wind.

The initial model was created using cross sections from the motion capture described in Section 4.3 and the aerodynamic design team's prior experience. Various CFD visualization tools including surface plots and flow trajectories were utilized to identify areas where the models could be improved. The analysis and refinement were then repeated until the design was satisfactory. This year's vehicle is narrower than last year's because refinements to the rider cavity modeling processes allowed tolerances to be tightened, and riders indicated that having some extra room within the fairing did little to improve comfort or handling. Due to the position of the rider being lower than in the 2010 Ragnarök, a more gradually tapered tail was found to be aerodynamically advantageous, providing more space for an independent frame. Changes in shipping constraints also allowed the fairing to be extended 6 in (150 mm). Using the drag force values calculated in each of the FloWorks simulations, the C_dA was calculated using Equation 5.

$$F_d = C_d A_{\text{frontal}} \rho \frac{V^2}{2} \quad 5$$

Table G shows the results of the CFD analysis. The resulting combined C_dA for the 2011 Helios is significantly improved over the 2010 Ragnarök due to the smaller frontal area and improved test case resolution in the design process.

Table G: Summary of CFD Results

Model	Drag Force, <i>lb</i> (<i>N</i>)	C_dA , <i>ft</i> ² (<i>m</i> ²)
2010 Ragnarök	2.19 (9.75)	0.412 (0.0383)

2011 Initial	2.22 (9.89)	0.418 (0.0389)
2011 Intermediate	2 (8.9)	0.377 (0.035)
2010 Final	1.91 (8.49)	0.359 (0.0334)

3.8 Roll-Bar Analysis

3.8.1 Simple Mechanical Model

The HPVT performed an analytical analysis of the rollover protection system using Castigliano's Method for beam deflection. An analytical approach required that the complex geometry of the roll bar be approximated by a simpler model. The curves of the roll bar were approximated by a member with straight sides and right angles with similar overall dimensions. The roll bar mounts were treated as fixed mounts, constraining each bottom of the member with two forces and a moment. For the side load, the roll bar was constrained opposite the applied load. Lastly, the cross-section of the roll-bar was approximated as a hollow rectangular section, imitating the position of the loading-bearing carbon fibers around the hollow honeycomb core. Figure ___ below shows the simplified model of the roll-bar.

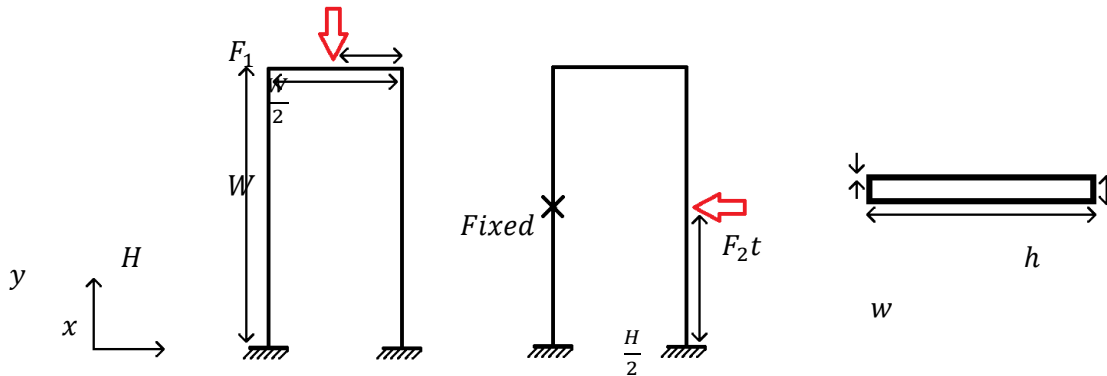


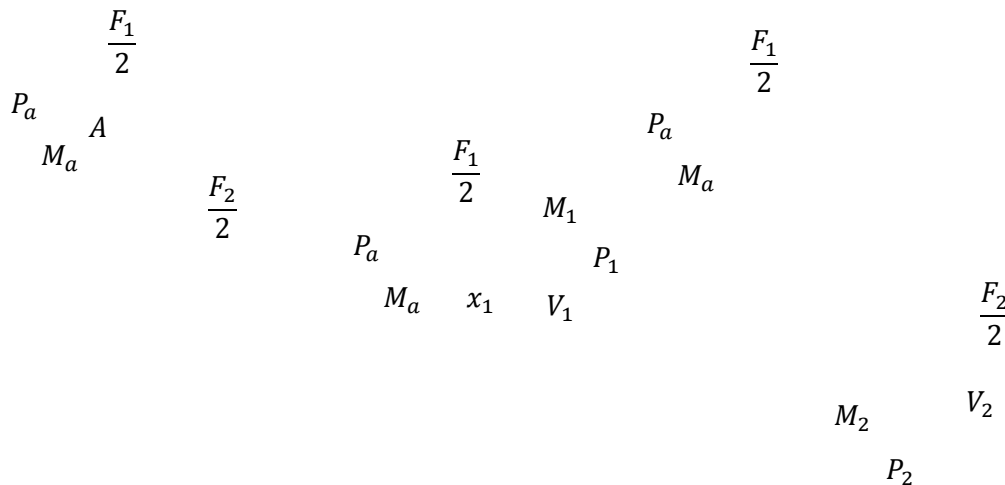
Figure 12: Model of roll bar top loading (left), side loading (center), and cross-section (right)

Equations 6 and 7, below, show how the area, A , and moment of inertia, I_o , of the cross-section were calculated.

$$A = w \cdot h - (w - 2 \cdot t) \cdot (h - 2 \cdot t) \quad 6$$

$$I_o = \frac{w \cdot (h^3 - (h - 2 \cdot t)^3)}{12} \quad 7$$

Due to the symmetry of the model, it can be simplified even further. One side of the roll-bar was analyzed under the assumption that it received half of the loading. The boundary conditions applied at the cut end of the member, point A, will preserve the presence of the opposing side of the roll bar. The first step of the analysis was to divide this simplified member into sections. Figure 13 shows the simplified model of the roll bar, along with the free body diagrams of these sections.



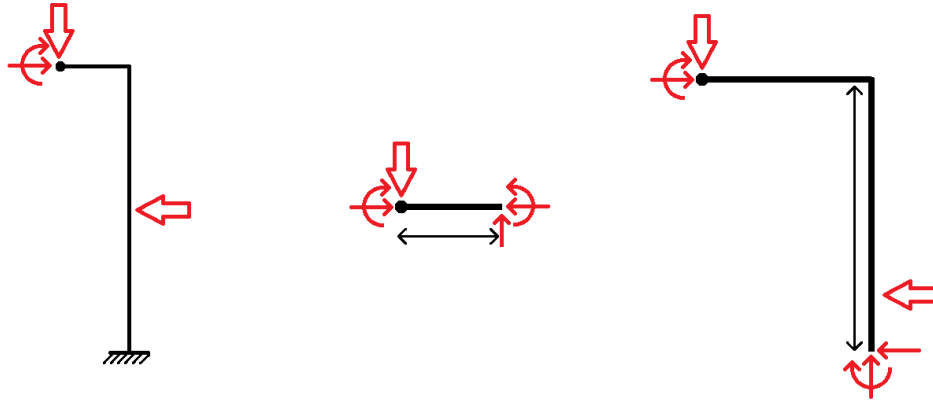


Figure 13: Half-model of roll bar loading (left) and free body diagrams for Section 1 (middle) and 2 (right) of the member.

Note that only one force, $\frac{F_1}{2}$ or $\frac{F_2}{2}$, was present in the model at one time during the analysis. Castigliano's Method was applied to this model twice, once for each load. Next, the principles of static equilibrium, shown below in equation 8, were applied to each section to solve for the six internal reactions as functions of P_a , M_a , and either $\frac{F_1}{2}$ or $\frac{F_2}{2}$, depending on which loading condition was being analyzed.

$$\sum F_x = 0, \quad \sum F_y = 0, \quad \sum_{\text{about } A} M = 0 \quad 8$$

Equation 9 shows the next step of the method, calculating the strain energy, U , that is stored in the member as a result of the internal reactions P_1 , P_2 , M_1 , and M_2 .

$$U = \int_0^{W/2} \frac{P_1^2}{2EA} dx_1 + \int_0^{W/2} \frac{M_1^2}{2EA} dx_1 + \int_0^H \frac{P_2^2}{2EI} dx_2 + \int_0^H \frac{M_2^2}{2EI} dx_2 \quad 9$$

The contributions to the strain energy from the internal reactions V_1 and V_2 were neglected. This is a common assumption to make when using this method due to the small amount of energy that is stored by shear deformation. Point A was held to the constraint that it had no deflection in the x -direction and a slope of zero. Equations 10 and 11 constrain the model to these conditions. $\delta_{x,A}$ is the deflection at point A in the x -direction and θ_A is the slope of the bend in the member at point A .

$$\delta_{x,A} = \frac{\partial U}{\partial P_A} = 0 \quad 10$$

$$\theta_A = \frac{\partial U}{\partial M_A} = 0 \quad 11$$

As a final step, the deflection in the member was calculated using either Equation 12 or Equation 13, depending on which loading condition was being analyzed.

$$\delta_{\text{top load}} = \frac{\partial U}{\partial F_1} \quad 12$$

$$\delta_{\text{side load}} = \frac{\partial U}{\partial F_2} \quad 13$$

The resulting predictions for the deflection of the rollover protection system were: $\delta_{\text{top load}} = 0.59$ in, $\delta_{\text{side load}} = 0.93$ in. Given these values, it can be predicted that the roll bar will not surpass the maximum allowable values for deflection given in the 2011 HPVC Rules.

3.8.2 Finite Element Analysis

A CAD model of the roll bar and the geometry relevant to mounting the roll bar to the frame was created for use in FEA to more accurately predict the behavior of the roll bar when under loading conditions specified in the HPVC rules and guidelines. Due to the complexity of layered composites, several minor idealizations were made in the modeling of the roll bar. The idealizations were as follows:

- 1) Material other than unidirectional carbon fiber was ignored, as the other materials were used for purposes other than strength.
- 2) The layering of the carbon fiber was ignored due to the immense amount of work required.
- 3) The Nomex rib was ignored in favor of a solid beam, which was designed such that it possessed an equivalent moment of area as found in the actual roll bar.
- 4) Mounting was accomplished by simply passing the tubes through the roll bar, as opposed to having mounting plates

For the purposes of simulation, the roll bar was modeled such that it had thin, flat sections in the locations on which the load would be applied. This was done so that loads could be precisely placed in the locations specified in the HPVC Rules and Guidelines.

The model of the roll bar was then put into an FEA program and subjected to top and side load conditions. For top loading conditions, a 600lbf (2.67kN) load at 12° toward the rear was applied on the top, with either end of the frame section secured rigidly. For side loading the roll bar was fixed opposite 300lbf (1.33kN) load. The deflections are reported in Table H. Figure 14 shows results of the analysis

Table H: Comparison of Hand Calculation and FEA Results

	Hand Calc. Results, in (mm)	ANSYS Workbench, in (mm)
Top Load	0.59 (14.99)	0.754 (19.15)
Side Load	0.93 (23.62)	1.207 (30.67)

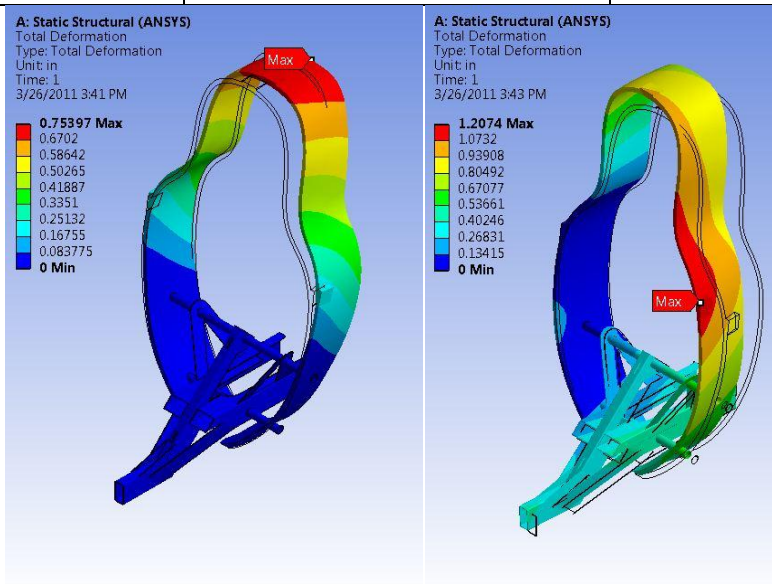


Figure 14: Deflection results of top (left) and side (right) loading conditions. Wireframe is of undeformed roll bar.

The deflection results from FEA closely match those found through hand calculations described in Section 3.8.1 and physical testing described in 4.6. All three results show that the roll bar passes the requirements for the RPS set forth by the HPVC rules and regulations [1].

3.9 Frame Analysis

3.9.1 Simple Mechanical Model

In order to prevent fairing and rider interference, a maximum tube size of 2 in was selected to be used in the construction of the frame. The bike was then modeled as a simply supported beam, with the distance from the rider’s center of gravity to the front tire being 17.5 in, and the distance from the rider’s center of gravity to the rear wheel being 29 in. The thickness required for a circular tube to support the load without yield with a factor of safety of 2 was then determined.

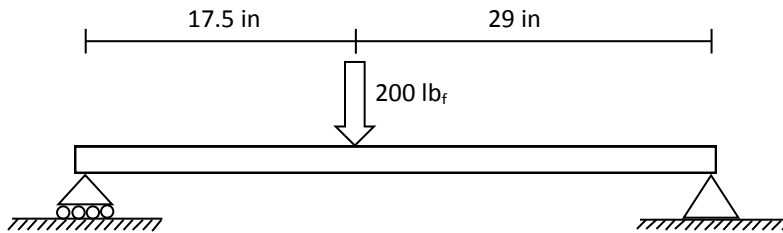


Figure 15: Simply Supported Beam Model

The maximum bending moment is found using Equation 14,

$$M_{max} = \frac{P \cdot a \cdot b}{L} \quad 14$$

where P is the 200 lb_f load, a and b are the lengths from the center of gravity to the wheels, and L is the length of the beam. This indicates that the maximum bending moment experienced by the beam is $2180 \text{ in} \cdot \text{lb}_f$. The required inner diameter is then calculated using Equation 15,

$$\sigma_{yield} = \frac{M \cdot y}{I} \quad 15$$

For material comparison, the team used MatWeb data for a 5086-H34 Aluminum (YS of 37.2ksi (256 MPa)), and 4130 chromoly steel (YS of 99.4 ksi (685 MPa)). The geometry of the tubing used for analysis is 1 in x 2 in (25.4 mm x 50.8 mm) rectangular tubing. For a 3104-H19 Aluminum tube, a wall thickness of 0.133 in (3.38 mm) would be required, which would make the tubing weigh 0.856 lb/ft (1.27 kg/m). For 4130 steel, a wall thickness of 0.043 in would be required, resulting in a tube weighing 0.848 lb/ft (1.26 kg/m).

Because of its superior strength to weight ratio and lower cost, the team chose to use 4130 steel as the construction material for the frame. The specified 4130 yield strength of 87.9 ksi (606 MPa) was used to calculate the frame's factor of safety.

3.9.2 Finite Element Analysis

To begin designing the geometry of the frame, data from power chair testing was analyzed to give the seat angle, and wheel positions were decided upon to optimize handling characteristics. The frame was then loaded and constrained as shown in Figure 16.

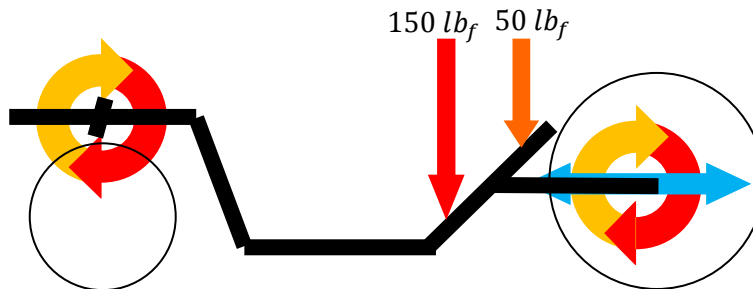


Figure 16: Frame Profile with Loading Conditions and FEA Constraints

Each frame model that tested with FEA was constrained such that the front fork was stationary, but could rotate as indicated in Figure 16, and the rear wheel could move forward and backward, as well as rotate. To determine if a frame design was acceptably strong for competition in the ASME HPVC, each frame design was subject to two distinct loading conditions with separate criteria for acceptability. The first loading condition was for a rider sitting on the bike, as shown in Figure 16: It was assumed that a normally situated individual would place 75% of their weight upon the bottom of their seat, with the remaining 25% being supported by their upper back. For the sake of simulation, a 200 lbf rider was used. A frame was considered passing if the minimum factor of safety on the vehicle was 2 for yielding with a shock loading value of 3 for normal loading.

The second loading condition was for the 600 lbf top load at 12° towards the rear exerted upon the roll bar support structure as shown in Figure 17.

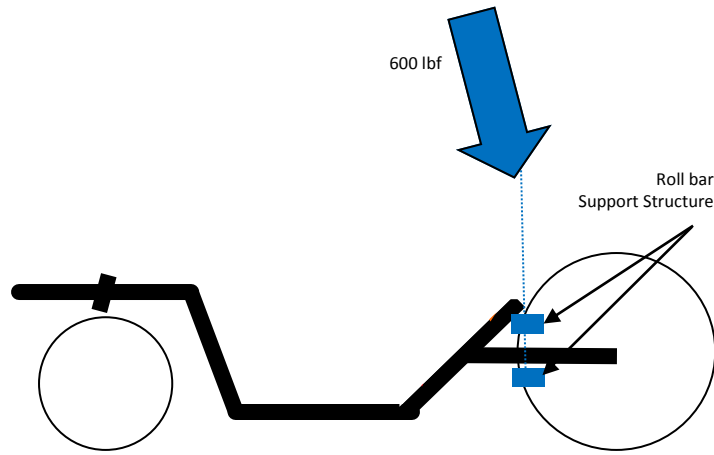


Figure 17: Loaded Roll Bar

A frame was considered passing if it could sustain this loading condition with a minimum factor of safety of 2 for yielding. No shock loading factor was used in calculating this safety factor, because the specified 600 lb_f is assumed to be an impact load.

As mentioned section 2.4.2, early frames used round tubing, but were more difficult to manufacture and had large stress concentrations at the welds. Furthermore, standard rear bicycle forks were difficult to model properly, diminishing the validity of the FEA.

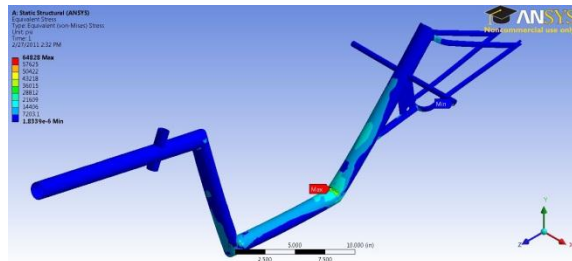


Figure 18: Round Tube Frame

The frame was later switched to rectangular tubing, which greatly increased the strength of the frame under normal loading circumstances. However, early rectangular tubed versions proved unsatisfactory due to insufficient support of the roll bar support tubes, as well as stress concentrations in the ends of the rear flanges.

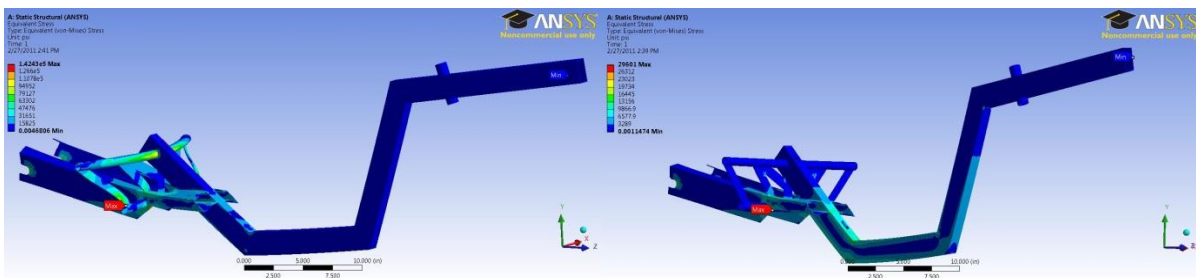


Figure 19: Roll bar (left) and Rider (right) loading conditions on an early rectangular tube frame

In the final design of the frame, the flanges mentioned previously continue down the bottom bar, redistributing the stress in the rear-wheel supports to the bottom bar, which previously saw very little stress. The roll bar support structure gained front-rear support with plates that attach to the top of the rear-wheel support structure.

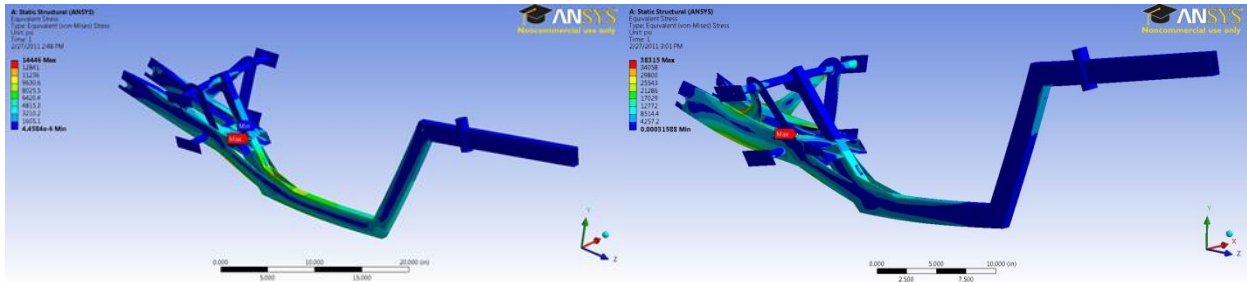


Figure 20: Roll bar (left) and Rider (right) loading conditions on an the final frame design

The factor of safety on the final frame is 6.0 for normal loading conditions, and 2.7 for rollbar loading conditions. As estimated by SolidWorks, the final weight is 10.75 lbf (47.8 N).

3.10 Analysis

An important consideration in the design of our vehicle is the monetary cost required to realize the design. Required testing, prototyping, and construction all contribute to the cost of the design. Each year, the team looks for ways to reduce cost. Reusing bicycle parts from previous vehicles, using donated items, finding cheaper materials, and reducing the amount of material used are a few of the common actions taken to reduce the cost of a design. This year, the team decided to detail the costs incurred during the year related to the design of the vehicle. In this way, the team can identify the areas with the largest expenses, and can begin to track the cost of the design from year-to-year. Table I below gives a short detail of the cost of the Helios.

Table I: Vehicle Cost Breakdown

	Materials/Parts	Consumables	Subtotal
Testing	\$179.57	\$1.58	\$181.15
Prototype	\$86.45		\$86.45
Mold Const. Vehicle	\$440.38	\$37.23	\$477.61
Const.	\$2,236.32	\$89.12	\$2,325.44
	Mat./Parts Cost	Consum. Cost	Total Cost:
	\$2,942.72	\$127.93	\$3,070.65

These costs are broken down in greater detail in Appendix 1. From our analysis, consumables were identified as having a relatively small contribution to the cost of the Helios. The largest cost was incurred by the construction of the vehicle, most of which was due to the use of composites. The steel frame in the Helios greatly reduced the amount of composites used compared to the team’s last three vehicles, reducing the overall cost of this vehicle.

3.11 Regenerative Braking

During competition, the regenerative braking system would be used in one of two ways. In the utility endurance competition, it would act as traditional regenerative braking, helping the rider to accelerate again after a stop. In the sprint event, it could be used as a power assist. In a power assist mode, stored power is used to increase top speed or help out with hill climbs. To analyze the usefulness of the system in both configurations, the team estimated 50% efficiency for the chain drive, motor, controller and battery.

The riders could activate the system early in the sprint event, unleashing the stored electricity during the time trap, ideally allowing the rider to go faster than would be possible using only pedaling. The second method in which a rider could use the system would be in the utility competition, where the system would act as a traditional regenerative braking system, saving kinetic energy for later use.

At a minimum, the system should be able to reasonably power the wheels with enough force to make up for its extra weight. For a 50% efficient, 20 lbf (9.07 kg) body to accelerate to 45 mph (20.1 m/s), it would require 5410 ft*lbf (3990 Nm) of kinetic energy.

Allowing a 200m (656 ft) generation distance means that the regenerative braking system would create 5411.2 ft*lbf / 656ft = 8.25 lbf of additional drag for the rider to overcome. Note that this is over three times the amount of drag

generated by a fully faired vehicle traveling at 45mph (Table F). This, along with the difficulty in reaching 45 mph in 300m, makes the system unusable during the sprint competition.

For utility competition purposes, a stop using solely the regenerative braking system from 30 mph would need a motor of 2500 W for an acceptable stopping time of 7.5 seconds. Motors of such power are too large and heavy to work in the Helios. However, if the Helios were to be sold as a production vehicle a regenerative braking system would be greatly beneficial. Having an electric assist would be a good selling point to many casual riders.

4 Testing

4.1 Optimal Cadence Testing

Testing was conducted to determine the optimal pedaling cadence of four riders on the Rose-Hulman team. The optimal pedaling cadence was defined as the cadence, or angular velocity of the bicycle crank arms, at which the rider could achieve a maximum aerobic power output.

To understand when each rider was reaching his or her respiratory limit, the volumetric flow rate of oxygen being exhaled, \dot{V}_{O_2} , was sampled as a rider completed an exhausting exercise regimen on a recumbent bicycle. As each rider increased his or her power output, the exhaled \dot{V}_{O_2} increased until his or her body was at its aerobic capacity, and the \dot{V}_{O_2} plateaued at a value of $\dot{V}_{O_2,max}$. The power data while the rider was at $\dot{V}_{O_2,max}$ was considered the rider's maximum aerobic power output. The test was repeated for each rider, with the rider maintaining a different cadence for each test, to gain an understanding of the power versus cadence relationship for each rider.

The riders pedaled a recumbent bicycle which was attached to a fluid trainer which is shown in Figure 21.

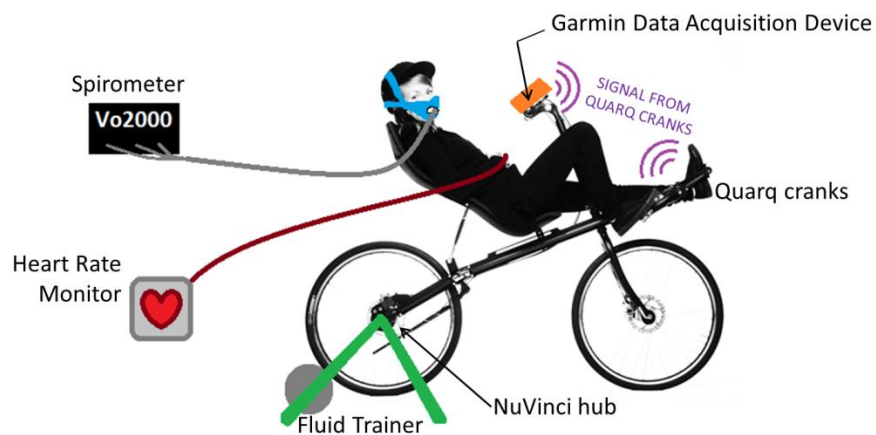


Figure 21: Experimental Set-up

The fluid trainer kept the bicycle in a stationary position and allowed the pedaling resistance to be changed by shifting gears on the bicycle. The recumbent was outfitted with a NuVinci internally geared Hub, which allows for infinite gear resolution within the range of the hub. The NuVinci allows the experimenters to dial in the resistance for the exercise regimen. Figure 22 shows a rider's power output for a theoretical exercise regimen.

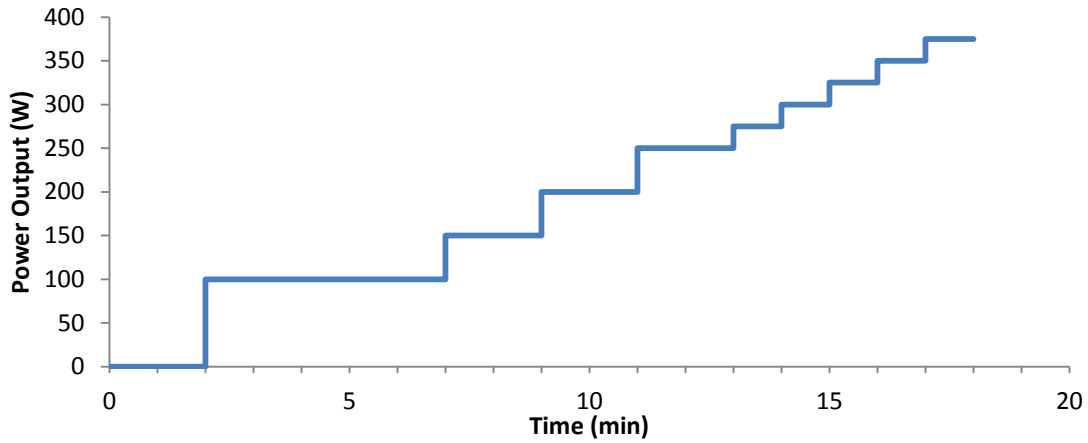


Figure 22: Power Increments for Sample $\dot{V}_{O_2,max}$ Exercise Test

The cadence and power were measured using a Quarq crankset, which wirelessly transmitted data to a Garmin device mounted on the handlebars. This allowed the rider and the experimenters to see the live data. The data was later downloaded from this device onto a computer for analysis. The rider's \dot{V}_{O_2} was measured by a Medgraphics VO2000 spirometer attached to a computer.

Based upon prior art, the power versus cadence relationship was expected to be a second order polynomial. Thus, each rider should have one cadence at which he or she is capable of producing a maximum amount of power. The final data from each rider was plotted and a polynomial curve was fit to the data. Figure 23 shows the fitted curves for the four riders.

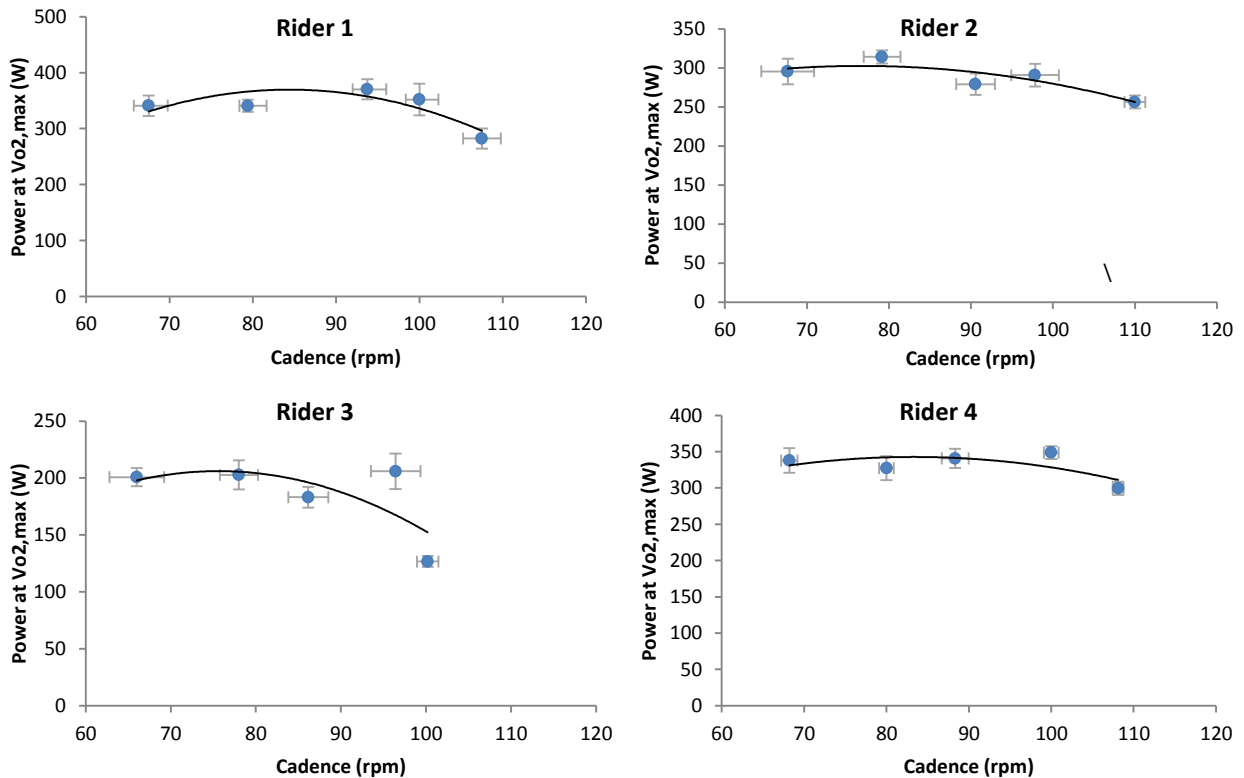


Figure 23: Maximum Power vs. Cadence Relationship for Each Rider

The optimum cadence for all riders on the team was between 75 and 85 rpm. Because the data looked similar we also ran an ANOVA analysis and a general regression on the data. The general regression showed that a second order model was valid for the data with a good fit ($R^2=87.2\%$). Although the general regression indicated a single optimum cadence for riders at 83 rpm, ANOVA revealed that the difference in riders' power at different cadences was not significant, except when the cadence was extremely high.

Table J: Predicted Power at Optimal Cadence

Rider	Predicted Power at Optimum Cadence (W)	Optimum Cadence (rpm)	Freely Chosen Cadence (rpm)	Difference (rpm)
1	370	83	78	+6
2	303	83	93	-10
3	206	83	91	-8
4	343	83	88	-5

Additional testing was performed without constraining the rider’s cadence and compared to the predicted optimal cadence. This found that while riders do not have statistically different power outputs over the range of cadences, most prefer the range 80-95. This range was used to develop the gearing as described in Section 3.3.

4.2 Seat Position

A test was performed to determine the optimum seat angle for the Helios. The optimal seat angle was defined as the seat angle that allowed riders to produce the highest average power during a one-minute sprint.

To measure the power output from the riders, a power chair was constructed that allowed riders to pedal in a position identical to the intended rider position for the Helios, except that the angle of the seat could be changed for this test. Riders drove a wheel with a PowerTap hub, and a kinetic fluid trainer provided resistance. Data from the PowerTap hub was collected with a Garmin Edge 500 bicycle computer and uploaded to a laptop through TrainingPeaks software.

Six team members with the potential to ride the Helios in competition were chosen for this test. Each rider was scheduled to ride the Power Chair at 5 different seat angles, in a random order. The range of seat angles was centered at the seat angle identified from power chair testing conducted by the team for the 2009 competition year, and extended to angles that riders felt were uncomfortably upright or recumbent. Testing occurred during a 5 day period. 4 data points could not be collected during this period and were abandoned. This created a larger uncertainty in the results for this experiment, but not every data point is necessary for the intended analysis.

During a test, a rider was given time to stretch, and then warmed up on the Power Chair at a very low power output. The rider then ramped up to the power output that he/she felt could be held for one minute. The data acquisition was started, then stopped one minute later, and the rider was allowed to cool down on the Power Chair. The average of the power output measured during this one minute was recorded.

After data was collected, an Anderson-Darling normality test was performed. The Anderson-Darling test gave a p-value of 0.264, which is greater than 0.05. This means that the data is believably normal and it is acceptable to use an ANOVA test on this data. An ANOVA test was performed to determine if the data sets collected at each seat angle were statistically different. For this test, a target p-value of 0.1 was chosen to better avoid the possibility of finding two seat angles to be the same if they really are different. It was determined that only the 50.5 degree from horizontal seat angle produced statistically different results. Figure 24, below, is the main effects plot for the seat angle. This plot shows the average effect that seat angle has on power output across all riders. From this plot, it can be determined that the 50.5 degree seat angle produces lower power output, and all other data points produce higher power output.

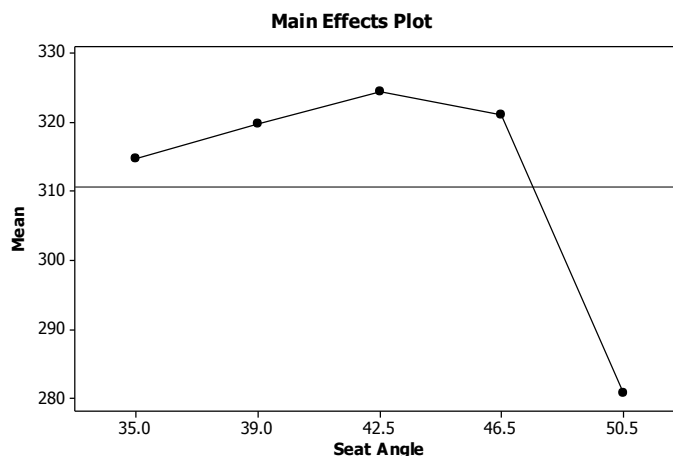


Figure 24: The main effects plot for Seat Angle, produced by an ANOVA test.

From this test, it was determined that the seat angle for the Helios should be between 35.0 and 46.5 degrees and not have a significant effect on the power output of the rider. The seat angle was selected from within this range to satisfy the other design criteria. The exact seat angle used of 44 degrees for the Helios will be chosen based on other design parameters, such as reducing frontal area and ensuring that the rider has vision of the race track.

4.3 3-Dimensional Motion Capture Testing

Motion capture testing was conducted to ensure reasonable clearances between the rider and the fairing. Data was collected from four test subjects riding a recumbent trainer. Qualisys Track Manager was used with three IR cameras, which recorded the three-dimensional positions of reflective balls worn on the joints of each rider. Because motion capture testing conducted by the team for the 2010 Ragnarök showed that pedaling motion differed with speed, each rider was recorded as they started to pedal, maintained a comfortable long-distance pace, and then sprinted.

A MATLAB program was then used to convert these sets of points into cross-sections of the space the riders used. First it generated sets of points to represent the joints and shoes. A convex hull algorithm was then used to find the smallest convex polyhedron that would encompass these points, as shown in Figure 25.

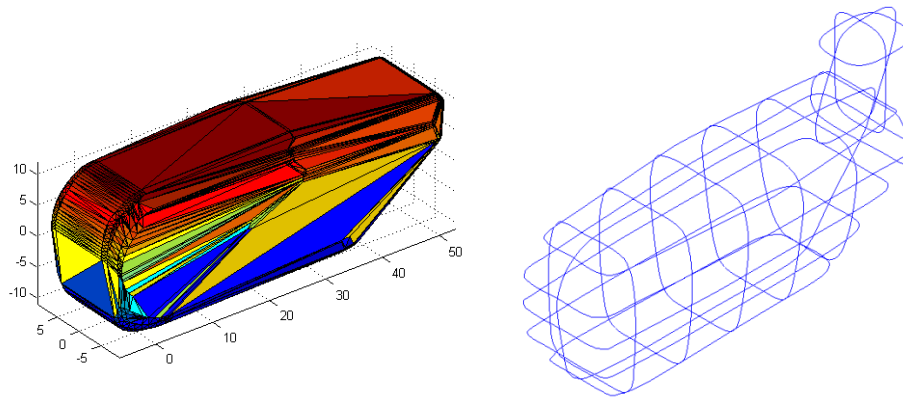


Figure 25: Convex Hull of Rider Space and Wire-Frame Model

The head and helmet were modeled separately. Once the required space had been found, cross sections were generated and saved in files which could be imported by SolidWorks, generating the Wire-Frame Model shown in Figure 25.

4.4 Fairing Mounting Testing

Applying a single sheet of carbon over a metal plate, as shown in Figure 26, was tested as a possible roll bar attachment method.

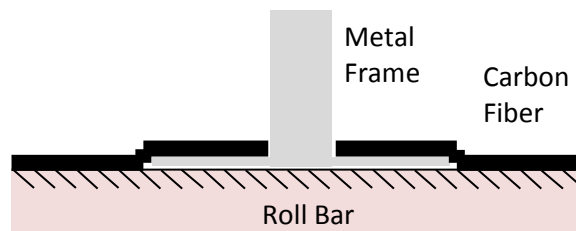


Figure 26: Diagram of tested attachment method

To test this design, 2 in by 3 in plates were covered by 4 in squares of 11 oz carbon fiber weave, then subjected to a tensile load through the use of a tensile tester. The samples failed as shown in Table K.

Table K: Failure Data

	Max Load	Load at First Delamination
Test A	-407.1	-171.7
Test B	-449.2	-200.4
Test C	-404.3	-78.1
Mean	-420.2	-150.07

Because the rules regarding the RPS consider delamination during testing to be a failure, this method of attaching the roll bar to the frame was discarded in favor the method discussed in Section 2.4.3.

4.5 Kevlar Zylon Testing

In 2009, the team performed testing which showed that adding a layer of Kevlar to the inside of a carbon fiber fairing improves rider safety in the event of a serious collision [5]. In the event that the fairing was damaged in a collision, the Kevlar would prevent sharp shards of broken carbon from injuring the rider. In 2010, the team opted to use a newer material called Zylon instead of Kevlar. Using Zylon would theoretically make the composite structure stronger due to the material’s high strength and stiffness. After repeating the carbon shard breakthrough test that was performed previously, the team found that Zylon was also effective at protecting the rider in the event of a collision [3]. However, members of the 2010 team reported that the Zylon was much more difficult to work with than Kevlar. Also, because of the much tighter weave pattern, the Zylon did not seem to become fully impregnated with resin, resulting in common delamination failures.

To determine if the Zylon actually resulted in a stronger composite structure, a four point bend test was performed. Material samples consisted of one layer of 11 oz carbon fiber, a 0.75 inch thick Nomex honeycomb rib, a second layer of 11 oz carbon fiber, and one layer of Kevlar or Zylon. The results are shown in Table L.

Table L: Tensile Test Results

	Ultimate Bending Strength (lb_f)	Average (lb_f)	Standard Deviation
Kevlar 1	468	666	173
Kevlar 2	788		
Kevlar 3	743		
Zylon 1	419	540	138
Zylon 2	691		
Zylon 3	510		

In the samples tested, failure occurred when the two layers of carbon fiber began to delaminate from each other. Although the average strength of the Zylon was greater than the average strength of the Kevlar, there was too much variation for the results to be conclusive. Because the test results did not show a significant difference between the bending strength of the two composite samples, the team decided to use Kevlar to line the interior of the fairing due to the ease of manufacture with this material.

4.6 Roll Cage Testing

The main method of rollover protection used by the Helios is a composite roll bar rigidly attached to the steel frame. The team assembled a mock roll bar and mounted it on a testing jig which accurately modeled the geometry and material on which the roll bar would be attached. A mock composite roll bar was then assembled in the exact method of the roll bar that will appear on the final vehicle.

To ensure the safety of the rider, the ASME HPVC rules stipulate that a roll bar be able to withstand $600 lb_f$ (2670 N) in a top loading at 12° towards the rear with a maximum of 2 in (5.08 cm) deflection, as well as a $300 lb_f$ (1330 N) side load applied at the shoulders with a maximum deflection of 1.5in (3.81cm), and that there be no evidence of permanent deformation or delamination in either the frame or the roll bar. The mock roll bar was subjected to these loading conditions in a tensile test machine. The roll bar withstood the top loading condition with a deflection of only 0.90 in (2.286 cm). The roll bar then withstood the side loading condition with a deflection of 1.22 in (3.10 cm). Most of this deflection was observed to occur in a 0.75 in (1.91 cm) thick section of foam that was part of the test fixture.

No visual or audible signs of damage were detected during and after the test, including in the mock roll bar jig. Furthermore, as seen in Figure 27, the plots of displacement versus load for both tests reveal very smooth curves.

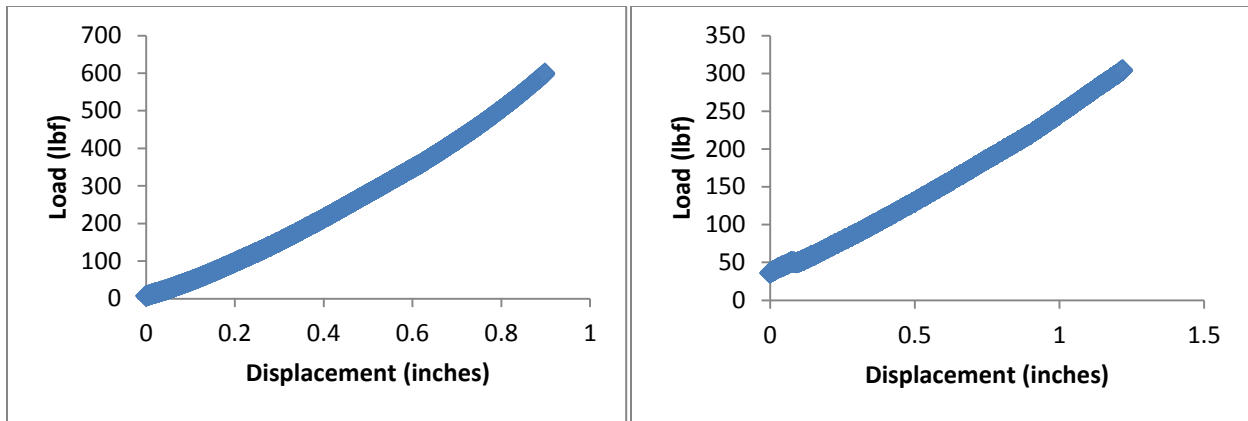


Figure 27: Plots of the data captured from Roll bar testing in top loading (left) and side loading (right) conditions

If the curves instead possessed sharp drops, it would indicate that failure (likely due to delamination) had occurred. This evidence is useful in analysis of roll bar damage, as it allows the team to detect faults such as delamination that would otherwise be difficult or impossible to detect. Because of the evidence outlined, the team feels that the roll bar for the Helios meets the criteria that *“there is no indication of permanent deformation, fracture or delamination on either the roll bar or the vehicle frame”* [1]

Upon determining that the roll bar passed the criteria set forth by the official ASME HPVC rules and guidelines, the team set forth to determine at which point the roll bar would fail either due to damage or deflection. The team decided to focus on the top loading condition, as an extreme top impact on the roll bar is more likely to occur during competition than an extreme side impact. As with the previous top loading test, the mock roll bar was placed into the tensile tester, but this time the tester was set to run until 2 in of deflection was achieved. The test generated the results seen in Figure 28.

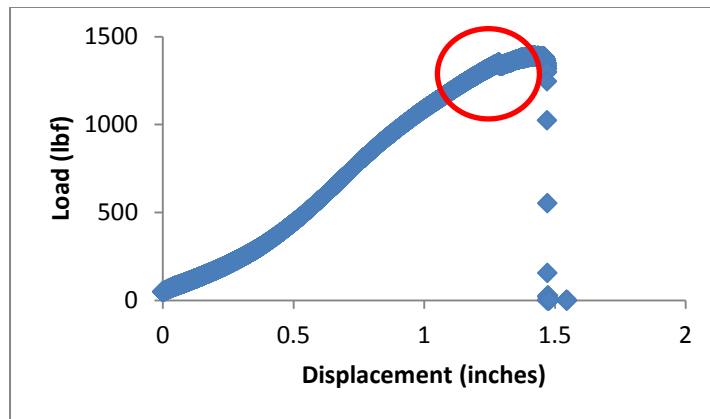


Figure 28: Data captured when testing roll bar to failure

A small but sudden dip occurred in the circled area in Figure 28. In the area circled, the load suddenly dropped by 16.1lbf (71.6 N) over the course of a deflection of 0.00469 in (0.0119 cm), leading the team to conclude that a small delamination failure occurred at a load of 1351lbf (6010 N). The roll bar went on to support 1390lbf (6180 N) before failing due to buckling

4.7 Universal Joint and Stability Testing

A prototype was built to validate the steering geometry and universal joint designs. Riders were asked to test the bike with various amounts of fork offset and provide their feedback. In building this prototype, it was discovered that a remote tiller system was required to achieve the proper handlebar length with the handlebars in a comfortable position. Once this had been accomplished, all riders reported that high speed handling was good, but that the vehicle was unstable at low speeds. Additionally, riders noted that various components were coming loose, introducing play into the system. Because play was more likely to affect low speed handling than high speed handling, the remote tiller system was rebuilt to significantly reduce this problem, including redesigning several components. Stability was then re-tested, and all riders approved of the handling at both high and low speeds. Further improvements to the mechanism, including reduced part count, will ensure good handling on the final vehicle.

The universal joint virtually eliminated issues with torque steer without degrading power transfer. However, over time the shaft of the universal joint began to wear where it contacted the needle bearings. To prevent this from occurring on the final vehicle, the universal joint shaft will be polished, and the interface lubricated. Prototyping also helped identify ways to improve the fit and reduce weight.



Figure 29: Prototype Universal Joint and Remote Tiller

4.8 Speedplay Frog Cleats

In previous years, the team has used Speedplay pedals, which are not designed to be practical for anything other than pedaling a bicycle. To improve practicality we explored different clipless pedal options, primarily Shimano SPDs and Speedplay Frog cleats, which are designed so that riders can also walk in them. Using a decision matrix, we identified Speedplay Frog cleats as the optimal choice. One of the primary reasons that the Speedplay Frog cleats ranked better than the Shimano SPD cleats is that they are free floating, which means the riders' heels can be moved side to side if necessary to avoid striking the fairing or derailleur.

5 Practicality

Helios is ultimately a single person form of transportation designed to be fast, efficient, adaptable to various conditions, and able to hold small amounts of cargo. Fabricated from composite materials and having an internal frame of steel, Helios's overall structure is corrosion resistant. Our use of standard bicycle parts allows minor repairs to be made in the same way as performed on upright bicycles. The design also takes into account the fact that those in the recumbent cycling community enjoy using them for commutes and participating in races (e.g., those sponsored by Human Powered Race America), and because of this Helios's rear wheel is replaceable with a custom leaning tricycle mechanism. The landing gear mechanism allows the rider to choose between being locked upright for low-speed situations or be unlocked for high speed turning. With this adaptability and the removability of the front wheel, Helios is easily disassembled for transport or compact storage.

5.1 Conditions

Helios is most useful when the temperature inside the vehicle remains between 41°F (5°C) and 95°F (35°C). The lower end of this range can be combated by riding with the fairing on and wearing cold weather gear to insulate the rider. For higher temperatures the fairing can be removed to allow for increased airflow and comfort for the rider. With the common ambient temperatures of Earth being from 32°F-95°F (0°C-35°C) and the fairing protecting the rider from precipitation, Helios is ride-able more than 320 days per year. The geographical range in which the Helios is ride-able for most of the year begins as far north as Michigan and Oregon and continues as far south as Florida [6,7]. The vehicle would be ride-able outside this region, but would be limited by temperatures. In Terre Haute, Indiana—the Team's location—the Helios would be ride-able approximately 330 days per year. The most likely cause for poor riding conditions is extreme cold in January.

The warmest month in Terre Haute is July with an average daily high temperature of 87°F (31°C) [8]. This temperature falls within the range specified above. Because of its ability to shed most of its fairing, the Helios would be able to allow maximum airflow to the rider during these hot days.

During the months of December, January and February, the mean monthly temperatures are too cold to comfortably ride a bicycle, with the coldest month being January, having an average temperature of 26°F (-3°C) [8]. When riding the

Helios fully faired, with the NACA duct sealed, the team estimates that after five minutes of biking, the inside temperature would exceed the outside temperature by at least 10°F (6°C). Analysis of cold temperature riding was not performed using average low temperatures, as these temperatures generally occur in the middle of the night, when people are unlikely to travel by bicycle

The biggest issue during the winter months would be the road salt applied to roads and bike trails and its effect on both the bicycle frame and components. To prevent corrosion on the bicycle frame, every surface of the frame is painted with weather-resistant paint. The team recommends that users of the Helios perform at least one complete teardown annually to inspect all parts of the bike for signs of wear and corrosion. Also recommended are quarterly inspections of both the braking and drive systems to ensure proper alignment of components.

During precipitation, riders close the top to prevent rain or snow from wetting the rider. Furthermore, during rain or snow, the rider can also install the tilting tricycle attachment described in 2.4.1.1 for increased stability on slick surfaces.

5.2 Visibility

Because safety is vital to the practicality of the vehicle, adequate visibility for the rider is a must. The rider is given more than 180° of clear line of sight. As with modern vehicles on the roadways today the team also mounted mirrors to the fairing to provide a visibility that approaches 320°. These features give the rider greater confidence in navigation of roadways and obstacles and dramatically increases safety by reducing the likelihood of a crash.

5.3 Utility Features

Helios as an unrestricted class vehicle has some added features to increase its practicality. In order to meet the minimum requirements for riding after dark in the state of Indiana the team intends to install a white light on the front of the vehicle visible from 500 ft (152 m) and a red light or red reflectors on the rear that is also visible from 500 ft (152 m). A bell or sounding mechanism will be installed to allow the rider to alert others of the vehicle or hazards. Removable mudguards will be developed for the single rear wheel for bike mode. A removable cover for the rear wheel hole when using the bike in tricycle mode will also be developed. Finally, for theft protection a conventional bicycle lock can be used to secure Helios to an object or prevent a rear wheel from freely rolling.

5.4 Special Features

A bladder-type water bottle will be installed in the vehicle. The rider would have convenient access to the bite valve by routing the tubing to a proper location. The bladder system will be easily accessible for pit stops. As the rider will need to replace electrolytes and carbohydrates, a small pocket for food and drinks has been placed within easy access of the rider.

As with any reliable commuting vehicle, minor repairs must be performable along the roadside from time to time. For this we will place a basic bicycle repair kit within the body of the bike. Included inside would be spare tubes, a chain breaker, and a multi-tool applicable to the systems of the bike. An air pump can also be placed behind the seat to provide air for the tires when needed.

Another special feature is the addition of a NACA duct directly in front of the windshield that opens downwards into the vehicle acting as an air scoop. This allows the vehicle to obtain the increased airflow needed during long distance events, but this duct can be closed during fast sprints to prevent increased drag caused by the airflow.

The rider will have a bicycle computer for monitoring cadence and speed as a measure of performance.

Our design of Helios has been intentionally made to meet the standards of HPRA to allow the consumer to compete in that organization's sponsored events.

6 Safety

Rider safety was an important constraint in all design decisions. The fairing ribs and mounting system were designed to ensure that the rider is protected in the event of a crash. A carbon-Kevlar hybrid was used for abrasion resistance, and fairing materials were selected to ensure that any vehicle damage would not create hazardous conditions within the vehicle. This was achieved through the use of a Kevlar weave, which prevents carbon shards from creating sharp edges within the fairing.

Stability improvements help the rider to avoid crashing. The rider's field of view has been designed to ensure that they can see their surroundings and react to them. Lights and reflective tape help to ensure that the Helios is easily visible to other vehicles. Hydration and ventilation have been included to aid in preventing heat sickness.

6.1 Communication

Even with the attempts to maximize rider visibility outlined in Sections 5.2, there may be situations when the rider is not aware of obstacles on the course, which can lead to unsafe situations sometimes resulting in crashes. In an attempt to minimize such occurrences, the HVPT will be using a collection of two-way radios to communicate between the team and the riders. There will be a two-way radio inside the bike. This will allow for clear communication.

6.2 Rider Elbow Protection

Included in the Helios' rollover protection system are composite shields that extend forward from the roll bar to protect the rider's shoulders and elbows from abrasion. These composite shields are integrated into the fixed rear fairing of the vehicle to protect the rider even when the full fairing is not present. The outside of these shields are covered in carbon-Kevlar hybrid fabric for abrasion resistance to protect the rider while sliding.

Materials/Parts

Consumables

Testing	Carbon Fiber	\$107.50	Plastic Cups	\$0.58
	Kevlar	\$23.00	Rubber Gloves	\$1.00
	Hybrid Fabric	\$8.13		
	Zylon	\$24.50		
	Epoxy Resin	\$16.44		
	Testing Subtotal:	\$181.15		
Prototype	Steel	\$20.00		
	Hardware			
	Universal Joint	\$52.73		
	Roller-Bearings	\$13.72		
	Prototype Subtotal:	\$86.45		
Mold Construction	Polystyrene Boards	\$136.64	Rollers	\$7.96
	Foam Board Glue	\$19.92	Plastic Cups	\$2.91
	Plaster	\$3.65	Rubber Gloves	\$2.79
	Fiberglass Weave	\$66.00	Plastic Sheeting	\$8.80
	Epoxy Resin	\$32.80	Packaging Tape	\$2.19
	Fiberglass Mat	\$51.00	Mold-Release	\$4.25
	Polyester Resin	\$127.25	Sanding Disks	\$8.33
	Body Filler	\$3.12		
	Mold Const. Subtotal:	\$477.61		
Vehicle Construction	Steel	\$466.85	Cut-off Wheels	\$3.98
	Hardware		Rollers	\$9.95
	Universal Joint	\$52.73	Plastic Cups	\$6.79
	Roller-Bearings	\$13.72	Rubber Gloves	\$4.39
	Carbon Fiber	\$65.00	Plastic Sheeting	\$26.39
	Kevlar	\$865.00	Packaging Tape	\$8.75
	Hybrid Fabric	\$138.00	Mold-Release	\$21.22
	Epoxy Resin	\$98.63	Sealant Tape	\$7.65
	Fairing Compound	\$2.15		
	Bike Components	\$533.65		
	Polystyrene	\$0.59		
	Construction Subtotal:	\$2,325.44		
		Materials/Parts Total:	\$2,942.72	
	Consumables Total:	\$127.93		
	Total Cost of Design:	\$3,070.65		

Works Cited

- [1] American Society of Mechanical Engineers, 2010, "Rules for the 2011 Human Powered Vehicle Challenge," American Society of Mechanical Engineers, New York, NY.
- [2] Patterson, B., 2001, *Lords of the Chaining*, 3rd ed., Santa Maria, CA.
- [3] Rose-Hulman Institute of Technology Human Powered Vehicle Team, 2010, "2010 Rose-Hulman HPVT Design Report," Rose-Hulman Institute of Technology, Terre Haute, IN.
- [4] National Weather Service, 2009, "Observed Weather Reports," National Oceanic and Atmospheric Administration, Silver Spring, MD.
- [5] Rose-Hulman Institute of Technology Human Powered Vehicle Team, 2009, "2009 Rose-Hulman HPVT Design Report," Rose-Hulman Institute of Technology, Terre Haute, IN.
- [6] MapXL, Inc., 2009, "US temperature January map," MapXL, Inc., San Jose, CA.
- [7] MapXL, Inc., 2005, "USA Temperature Map July," MapXL, Inc., San Jose, CA.
- [8] The Weather Channel, 2011, "Monthly Averages for Terre Haute, IN (47809),".
- [9] Rose-Hulman Institute of Technology Human Powered Vehicle Team, 2008, "2008 Rose-Hulman HPVT Design Report," Rose-Hulman Institute of Technology, Terre Haute, IN.
- [10] Juvinall, R.C., and Marshek, K.M., 2006, *Fundamentals of Machine Component Design*, 4th ed., John Wiley & Sons, Inc, Hoboken, New Jersey, pp. 189-206.